Electron-phonon coupling superconductivity and tunable topological state in carbon-rich selenide monolayers

Panlong Kong,[1] Xiaotao Zhang,[1] Jingjing Wang,[2] Wenhui Tian,[2] Yuxiang Ni,[1] Bai Sun,[3]
Hongyan Wang,[1] Hui Wang,[1] Yuan Ping Feng,[4] and Yuanzheng Chen[1,*]
[1]*School of Physical Science and Technology, Southwest Jiaotong University, Chengdu 610031, China*
[2]*College of Computer and Information Engineering, Hubei Normal University, Huangshi 435002, China*
[3]*Frontier Institute of Science and Technology (FIST), Xi'an Jiaotong University, Xi'an, Shaanxi 710049, China*
[4]*Department of Physics and Centre for Advanced Two-Dimensional Materials, National University of Singapore, Singapore 117551, Singapore*

(Received 24 November 2022; revised 10 May 2023; accepted 16 May 2023; published 26 May 2023)

The coexistence of Dirac cones and Van Hove singularities (VHSs), as the notable feature on prominent electronic band structure in recently hot-topic Lieb lattice and twisted graphene superlattice materials, has recently drawn tremendous attention since it offers an ideal platform for realizing correlation-driven electronic states (e.g., superconductivity and topological state). Here, we have identified two two-dimensional (2D) crystals, namely C_4Se and C_5Se, which exhibit the coexistence of Dirac cones and VHSs. Based on *ab initio* calculations and the Bardeen-Cooper-Schrieffer theory, we investigated the electron-phonon coupling and possible superconductivity in both structures. The results indicate that C_4Se possesses intrinsic superconducting states, whereas C_5Se exhibits tunable superconductivity when doped. Their superconducting critical temperature (T_c) can reach up to 11.6 and 11.2 K, respectively, surpassing the majority of 2D superconductors. Besides, we uncovered an approximate Dirac cone in C_6Se with a small band gap of 0.17 eV. Via the application of a biaxial compressive strain, remarkably, the C_6Se can be transformed into a topological insulator. These findings highlight the potential of carbon-rich C-Se 2D crystals as a promising platform for investigating fascinating band structures and physical states, thus advancing our comprehension of 2D crystals.

DOI: 10.1103/PhysRevB.107.184115

I. INTRODUCTION

Graphene, as a typical two-dimensional (2D) crystal, has attracted significant attention since it was exfoliated from graphite in 2004 [1]. This pioneering work not only provided an effective way to discover other 2D crystals but also opened up a vast landscape of 2D materials with exotic physical phenomena and properties [2,3]. In addition to excellent mechanical properties, the distinctive Dirac cone band structure of graphene gives rise to several exceptional properties, including high carrier mobility [4], the presence of massless Dirac fermions [5], and high thermal conductivity [6]. Intriguingly, the superconducting properties in graphene can be achieved by means of doping [7], intercalation [8–10] and twisting [11], bringing its Fermi energy level close to Van Hove singularity (VHS) in the band structure. This is mainly due to the fact that the VHS near the Fermi surface makes the system inherently vulnerable to Fermi surface instability [12,13], and therefore could be considered as a small perturbation by producing positive effects in their electronic properties, such as charge, spin, and/or pairing susceptibilities, as well as serving as potential the origin of magnetism [14], superconductivity, and/or topological states [15,16] in the 2D materials.

Recently, the intriguing coexistence of the Dirac cone and VHS was reported in the electronic band structures of Lieb lattice materials [17–19]. This unique band feature provides an exciting platform for realizing correlated electronic states, such as superconductivity and topologically nontrivial states. For example, both unconventional superconductivity and Z_2 topological surface states were recently observed in Lieb lattice and twisted graphene [20–24]. Such remarkable phenomenon can be attributed to the special electronic band structure of these materials near the Fermi energy which drives the transitions to the emergent phases, e.g., superconductivity and/or topologically nontrivial states. However, known materials with the band structure feature—the coexistence of Dirac cones and VHSs—are quite limited, particularly in 2D crystal materials. It is thus crucial to design/discover 2D crystals with such band structures in order to investigate the correlation-driven exotic electronic states (i.e., superconductivity, topological states). In this regard, carbon-rich 2D composites could be promising candidates as discussed below. First, carbon-rich 2D crystals can inherit the Dirac cone of graphene, while the inclusion of other elements in the compounds may enhance the density of states (DOS) near the Fermi surface, leading to VHSs. Second, carbon-rich materials have the potential to exhibit superconductivity by coupling with high-frequency phonons. This coupling arises from the strong bonds and light mass of carbon, resulting in strong electron-phonon matrix elements [25–30].

---

[*] cyz@swjtu.edu.cn

Additionally, carbon-rich materials hold the possibility of topological states when V-VI elements (i.e., Se, Te, Sb, Bi) are integrated into the system [31–34].

As one of the chalcogenide compounds, selenium (Se) has been extensively studied in 2D selenides. Here, this work focuses on the design of Se-based 2D carbon-rich crystals (C-Se). As a result of extensive simulations, we identified three carbon-rich crystals (C_4Se, C_5Se, and C_6Se) with excellent thermal and dynamic stability. The first-principles calculations results reveal that the band structures of C_4Se and C_5Se both exhibit a Dirac cone–VHS coexisting feature, similar to that of the Lieb lattice and twisted graphene band, which are favorable to induce superconductivity. Our further simulations indicate the C_4Se manifests intrinsic superconducting states, while the C_5Se exhibits a zero band-gap semimetal feature but can be tuned into superconductivity through *p*-type doping. In addition, the C_6Se shows a strain-induced transition to a topological state at a critical compressive strain. The current findings offer a 2D crystal platform for realizing a Dirac-VHS band structure and correlation-driven exotic states.

II. METHOD

An extensive structure search for stable C_xSe ($x = 1$–6) compounds within 1–4 formula units has been carried out using the global search via particle-swarm optimization (PSO) algorithm, which was implemented in the CALYPSO package [35–37]. The effectiveness of this method in predicting the ground state structures of various materials is supported by experimental confirmation of many predicted structures [38–42]. *Ab initio* calculations based on density functional theory (DFT) were performed using the VASP code [43]. The projector-augmented wave (PAW) [44] approach was employed with a cutoff energy of 600 eV. The generalized gradient approximation (GGA) [45] of the Perdew-Burke-Ernzerhof (PBE) was used to treat the electronic exchange-correlation interaction, while the more accurate band gap was characterized by adopting the Heyd-Scuseria-Ernzerhof (HSE06) [46] hybrid functional. The Γ-centered Monkhorst-Pack grid with a *k*-point density of $2\pi \times 0.02\,\text{Å}^{-1}$ was adopted for the Brillouin zone (BZ) sampling [47]. The convergence thresholds for energy and force in structural optimization and self-consistency were determined to be 10^{-8} eV and 10^{-3} eV/Å, respectively.

The density functional perturbation theory (DFPT) [48] implemented in the QUANTUM ESPRESSO package [49,50] was used to compute the electron-phonon coupling (EPC) and superconductivity properties. Phonon calculations were carried out using the PBEsol form of the generalized gradient approximation (GGA) from the Standard Solid-State Pseudopotentials (SSSP) library [51], with a plane wave basis set cutoff of 80 Ry for kinetic energy and 800 Ry for charge density. The static calculation electron density was assessed using a $32 \times 32 \times 1$ *k* mesh, while a $16 \times 16 \times 1$ *q* mesh was adopted for both phonon and EPC calculations. The determination of the mode-resolved magnitude of EPC λ_{qv} follows the BCS theory [52],

$$\lambda_{qv} = \frac{\gamma_{qv}}{\pi h N(E_F)\omega_{qv}^2}, \tag{1}$$

where λ_{qv}, $N(E_F)$, and ω_{qv} represents the phonon linewidth, the electronic DOS at the Fermi level, and the phonon frequency, respectively. The γ_{qv} can be estimated by

$$\gamma_{qv} = \frac{2\pi\omega_{qv}}{\Omega_{\text{BZ}}}\sum \left|g^{v}_{kn,k+qm}\right|^2 \delta(\varepsilon_{kn} - \varepsilon_F)\delta(\varepsilon_{k+qm} - \varepsilon_F), \tag{2}$$

where Ω_{BZ} and $g^{v}_{kn,k+qm}$ denote the volume of BZ and the EPC matrix element, respectively, and ε_{kn} and ε_{k+qm} represent the Kohn-Sham energy. The $g^{v}_{kn,k+qm}$ can be achieved by adopting linear response theory [53], while the Eliashberg spectral function of the electron-phonon interaction $\alpha^2F(\omega)$ and the cumulative frequency-dependent EPC $\lambda(\omega)$ can be obtained via the following formula:

$$\alpha^2F(\omega) = \frac{1}{2\pi N(E_F)}\sum_{qv}\frac{\gamma_{qv}}{\omega_{qv}}\delta(\omega - \omega_{qv}) \tag{3}$$

and

$$\lambda(\omega) = 2\int_0^{\omega}\frac{\alpha^2F(\omega)}{\omega}d\omega, \tag{4}$$

respectively. The computation of the logarithmic average frequency $\omega_{\log}$ and the T_c can be achieved using the following expression:

$$\omega_{\log} = \exp\left[\frac{2}{\lambda}\int_0^{\infty}\frac{d\omega}{\omega}\alpha^2F(\omega)\log\omega\right] \tag{5}$$

and

$$T_c = \frac{\omega_{\log}}{1.2}\exp\left[-\frac{1.04(1+\lambda)}{\lambda - \mu^*(1+0.62\lambda)}\right]. \tag{6}$$

According to Eq. (2), the phonon linewidth arises from two major contributions, namely the EPC matrix elements and the Fermi surface nesting factor $\xi(q)$, which can be expressed as

$$\xi(q) = \sum_{k,n,m}\delta(\varepsilon_{kn} - \varepsilon_F)\delta(\varepsilon_{k+qm} - \varepsilon_F). \tag{7}$$

Employing the WANNIER90 package [54] interfaced with QUANTUM ESPRESSO, we performed calculations of the tight-binding (TB) matrix elements by projecting Bloch states onto maximally localized Wannier functions. The Wannier-Tools package [55] with iterative Green's function method was utilized to calculate the edge energy spectrum.

III. RESULTS AND DISCUSSION

A. Crystal structures

To identify the potential stable C-Se chemical stoichiometries and their crystal structures in 2D space, we adopt a first-principles swarm intelligence structure search to explore potential stable 2D crystal structures of C_xSe ($x = 1$–6) with varying cell size and layer thickness. Through this process, we successfully reproduced the previously reported $P3m1$ CSe structure [56], proving the reliability of this method, and three low-energy stable structures of C_4Se, C_5Se, and C_6Se were identified as shown in Figs. 1(a)–1(c). The predicted C_4Se, C_5Se, and C_6Se compounds adopt the orthogonal crystal structure with the $Pmm2$ symmetry, the trigonal crystal structure with the $P31m$ symmetry, and the orthogonal structure with the $P2_12_12$ symmetry, respectively. Note that we also

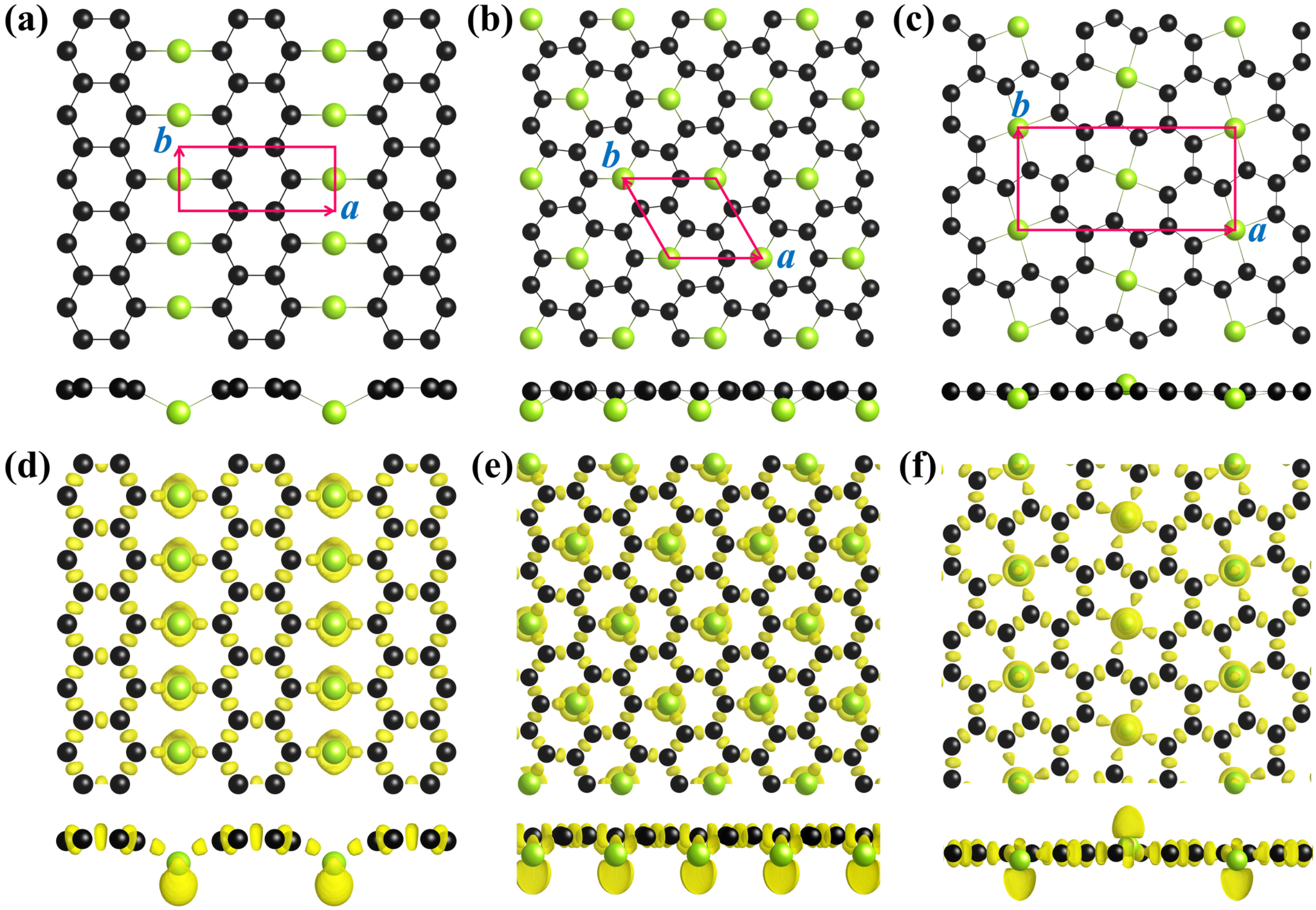

FIG. 1. Top and side views of (a)–(c) the optimized configurations and (d)–(f) the electron localization function (ELF) maps with an isosurface value of 0.83 a.u. of the *Pmm*2 C_4Se, *P*31*m* C_5Se, and $P2_12_12$ C_6Se. Black and green balls represent C and Se atoms respectively.

find another low energy PC_6−type C_6Se configuration with $P-3$ symmetry, which has been reported and discussed by Springer *et al.* [57]. Thus, we only focus on the $P2_12_12$ C_6Se configuration in the following. The detailed crystal structural information of C_xSe ($x = 4, 5, 6$) is summarized in the Supplemental Material [58].

The C_4Se monolayer exhibits a distinctive configuration where all C atoms are two-coordinated with sp^2 hybridization, forming polybiphenyl units along the *b* direction [Fig. 1(a)], and each Se atom is attached to two C atoms on the benzene ring unit, forming sp^3 hybridization and fulfilling the chemical octet rule. The resulting structure consists of alternating polybiphenyl units and zigzag nonbonding Se chains, with a Se-Se distance of 2.56 Å between the two-nearest Se atoms that is beyond the range of Se-Se bonds. The basic building blocks of C_5Se are hexagons composed of five C atoms and one Se atom, where each Se atom is tricoordinated with C atoms and shared by three hexagons. In comparison with C_4Se and C_5Se, C_6Se has a complex configuration consisting of both pentagons and hexagons. Each Se is enclosed by four C atoms constituting two sets of diagonal pentagons and hexagons. In these structures, the average of the C-C bond length is almost the same as that of graphene (1.42 Å), while the length of the C-Se bond is slightly larger than that of the C-S bond in the CS monolayer (1.87 Å) [59,60]. To reveal the bonds' nature for these three monolayers, the electron localization function (ELF) is calculated and presented in Figs. 1(d)–1(f). The analysis demonstrates that the bonds between adjacent C atoms and between C and Se atoms in these structures are covalent. It is noteworthy that each Se atom possesses a nonbonding lone electron pair. The electronic or mechanical properties may exhibit directionality due to variations in the bonding patterns and atomic arrangements along the *a* and *b* directions.

B. Structural stability

To assess the stability of these proposed C-Se monolayers, we investigated their energetic relative stability by calculating the formation energy (E_f) and building the convex hull as illustrated in Fig. 2(a). We calculated the cohesive energies of the predicted three compounds and the obtained values (6.40 eV/atom for C_4Se, 6.43 eV/atom for C_5Se, and 6.54 eV/atom for C_6Se) are higher than some typically synthesized 2D materials, such as phosphorene (3.30 eV/atom) [61] and 2D MoS_2 (5.15 eV/atom) [62], and are comparable to that of BC_3 monolayer (6.86 eV/atom) [63] and PC_6 monolayer (6.98 eV/atom) [64]. These comparisons demonstrate that the C_4Se, C_5Se, and C_6Se monolayers have outstanding thermal stability and are likely to be synthesized for practical applications.

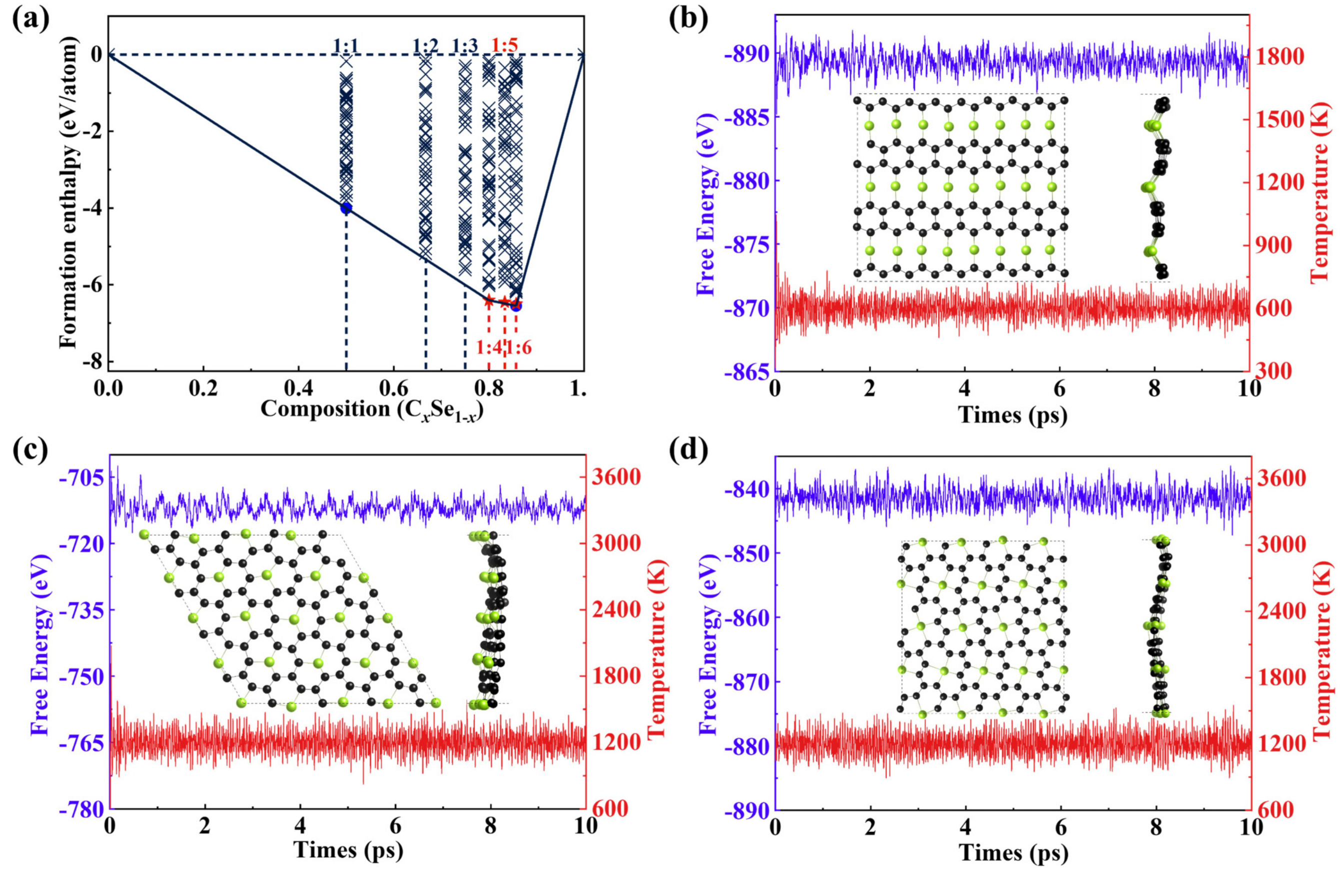

FIG. 2. (a) Formation energy (E_f) of C_xSe ($x = 1-6$) with respect to pure carbon and selenium at 0 K. Blue solid circles represent previously reported $P3m1$ CSe and $P-3$ C_6Se structures. Red solid stars represent predicted $Pmm2$ C_4Se, $P31m$ C_5Se, and $P2_12_12$ C_6Se structures. (b)–(d) The free energy and temperature fluctuations of C_4Se, C_5Se, and C_6Se with the time step of the molecular dynamics simulation. No drastic fluctuations are found, confirming that all structures are thermodynamically stable.

Additionally, we calculated the phonon dispersion curves of these structures, and verified their dynamics stability by the absence of any imaginary mode (see Supplemental Material Fig. S1 [58]), confirming the dynamics stability of the C_4Se, C_5Se, and C_6Se monolayers. The phonon projection band analysis shows that the low-frequency stretching modes are related to the strong coupling between Se and C atoms, while the high-frequency modes are mainly from the vibrations of C atoms. Moreover, the highest vibrational frequency of the C_4Se, C_5Se, and C_6Se monolayers reach 1452, 1416, and 1563 cm^{-1}, respectively, which are close to those of BC_3 (1450 cm^{-1}) [65], C_3S (1455 cm^{-1}) [66], and PC_6 (1529 cm^{-1}) [64], indicating strong chemical bonds between C atoms in these monolayers.

The structural stability at finite temperature was also analyzed from the perspective of *ab initio* molecular dynamics (AIMD). By using supercells of $4 \times 10 \times 1$ for C_4Se, $4 \times 4 \times 1$ for C_5Se, and $4 \times 6 \times 1$ for C_6Se, the molecular dynamics simulations were carried out for 10 ps with a 1-fs time step without symmetry constraints at temperatures of 300, 600, 900, and 1200 K, respectively. The results show that, at room temperature, all three structures maintain their structural integrity without significant distortions (shown in Supplemental Material Fig. S2 [58]), showing good thermal stability. With increasing the temperature, the C_4Se structure can retain its structural integrity without appreciable distortions up to 600 K, while the C_5Se and C_6Se structures show their thermal stability up to 1200 K, as shown in Figs. 2(b)–2(d). These simulations indicate that these monolayers are thermodynamically stable up to reasonably high temperatures.

To investigate the mechanical stability, the changes of energy with respect to the in-plane strain for the C_4Se, C_5Se, and C_6Se monolayers were calculated by using the standard Voigt notation. The calculated elastic constants are listed in the Supplemental Material [58] and meet the Born-Huang criteria of $C_{11} > |C_{12}| > 0$, $C_{66} > 0$ and $C_{11}C_{22}–C_{12}^2 > 0$, indicating the mechanical stability of these monolayers. By analyzing the orientation-dependent Young's modulus and Poisson's ratio (see Supplemental Material Fig. S3 [58]), we found that C_4Se and C_6Se have anisotropic mechanical properties contrary to the isotropic feature of C_5Se, and they all exhibit robust mechanical stiffness.

C. Coexistence of Dirac cone and VHS

The corresponding electronic band structures of C_4Se and C_5Se are shown in Figs. 3(a) and 3(b), respectively. For C_4Se, there are two linear bands (red and blue lines) crossing the Fermi level, resulting in inherent metallicity, which is also corroborated by the Fermi surface distributions along the high-symmetry paths [inset in Fig. 3(a)]. It is noteworthy that

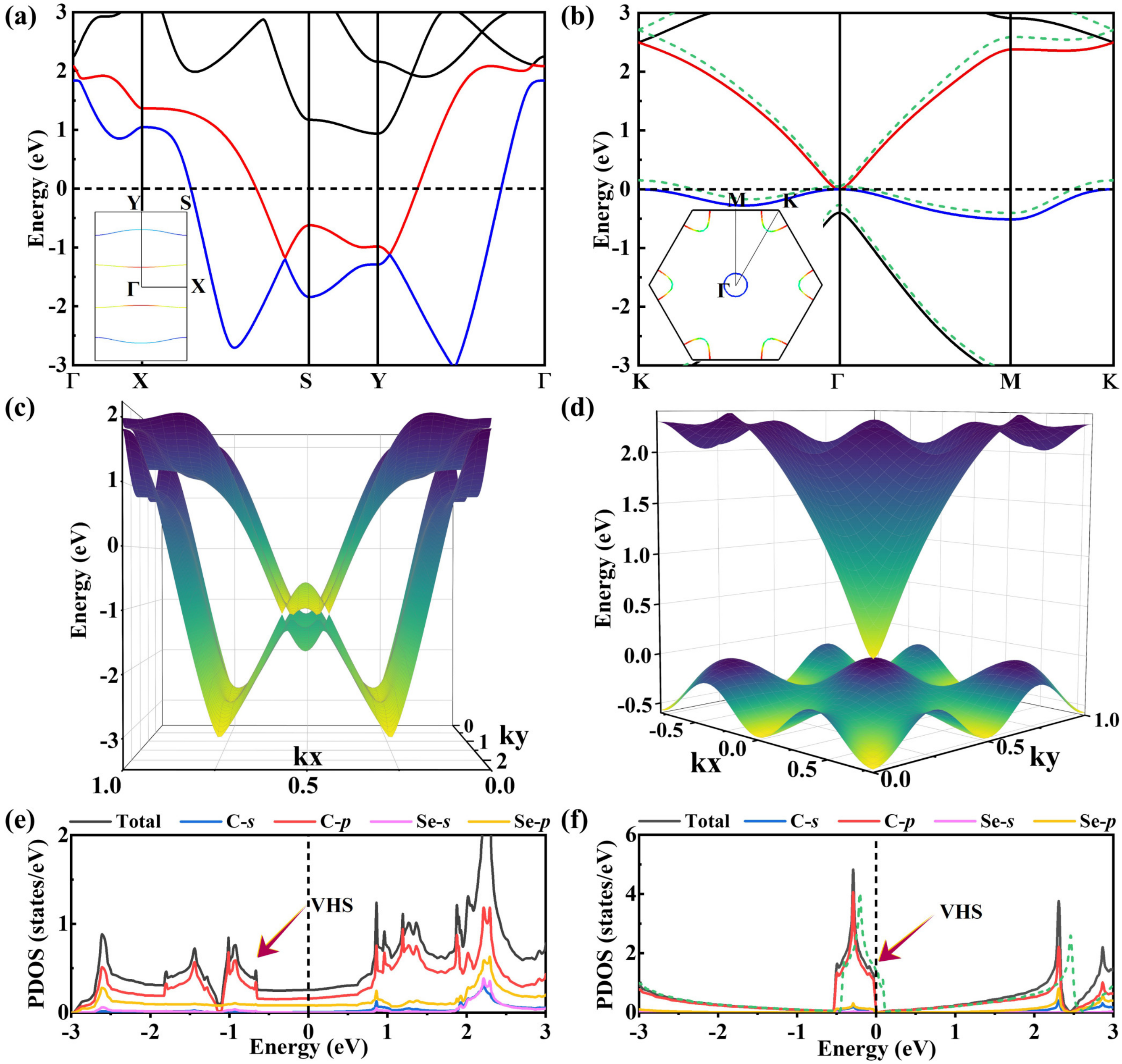

FIG. 3. (a) Electronic band structure of C_4Se. The inset is the Fermi surface of C_4Se. (b) Electronic band structures of pristine C_5Se (solid lines) and *p*-doped C_5Se (green dashed line). The inset is the Fermi surface of *p*-doped C_5Se. (c) 3D band structure of C_4Se. (d) 3D band structure of C_5Se. (e) PDOS of C_4Se. (f) PDOS of pristine C_5Se (solid lines) and total DOS of *p*-doped C_5Se (green).

the two linear bands form two Dirac cones along the *S*-*X* and *Y*-Γ paths in the BZ, which are situated at about 1.2 eV below the Fermi level. Unlike the double cone feature observed in C_4Se monolayer, C_5Se possesses only one quadratic band touching point, consisting of a single cone and a nearly flat band located close to the Fermi level. The quadratic band touching point is precisely located at the Fermi level on the Γ point, indicating that it is a semimetal with zero band gap [Fig. 3(b)]. This band structure is similar to that of the Lieb lattice, and the characteristics of the flat band near the Fermi level have also been seen in twisted graphene, which has important implications for the structural properties. The full 3D band dispersions of the C_4Se and C_5Se monolayers are shown in Figs. 3(c)–3(d), which provides a clear view of the unique band characteristics. From the analysis of atom-decomposed and orbital-decomposed band structures (see Supplemental Material Fig. S4 [58]), the bands of C_4Se and C_5Se near the Dirac point primarily originate from the C$-p_z$ orbitals. We compared their band structures obtained with PBE and HSE hybrid functionals. Negligible differences were found in the band structures for both C_4Se and C_5Se and the Dirac cones remain in the HSE band structures.

Moreover, the existence of a saddle point near the Fermi level in both C_4Se and C_5Se could result in a divergence in the DOS, known as VHS. This could amplify even weak interactions when the Fermi energy approaches the VHS, leading to instabilities and the emergence of matter with desirable properties. Using the linear-tetrahedron method, we obtain the

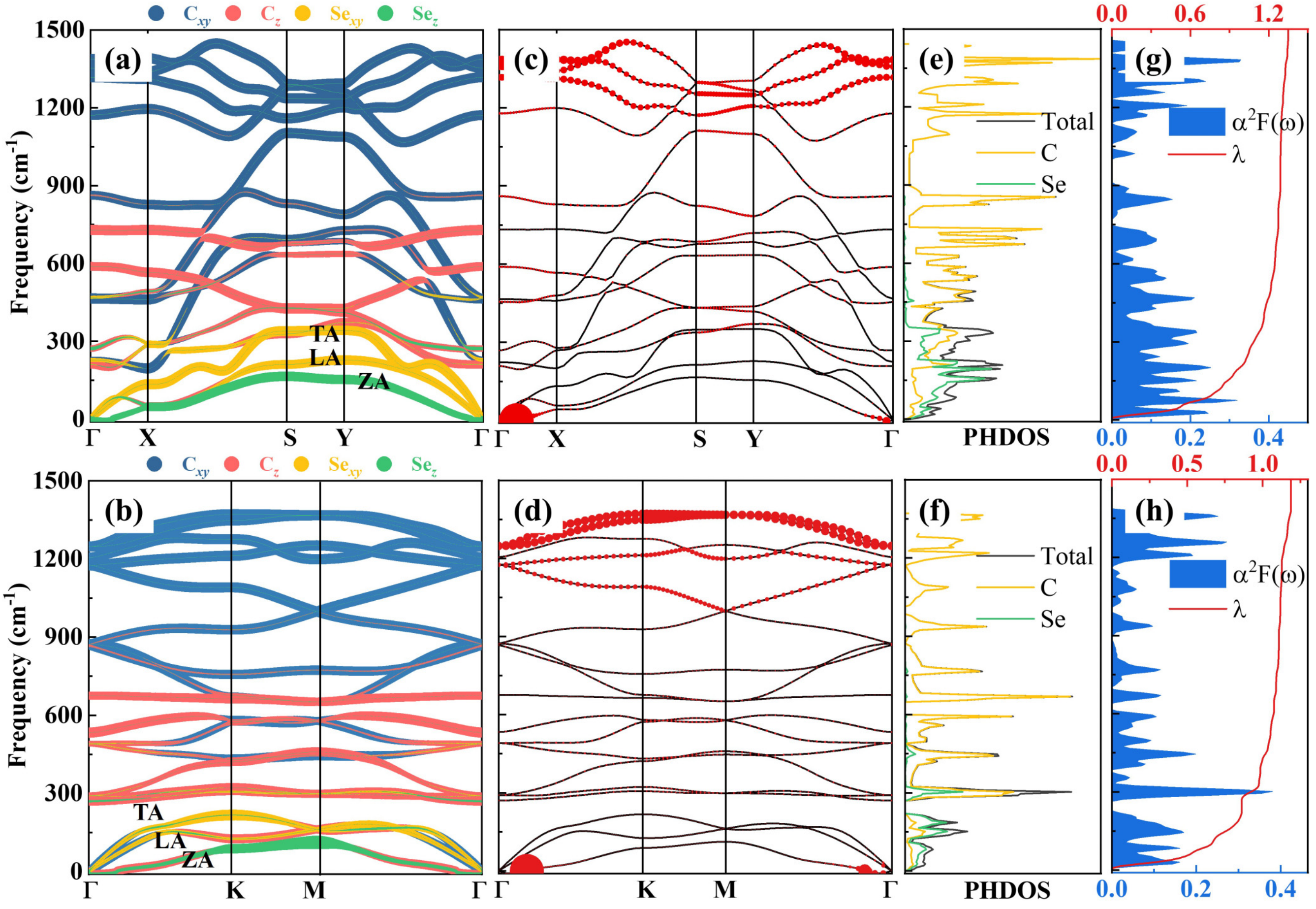

FIG. 4. (a),(b) The phonon dispersions, (c),(d) λ_{qv}, (e),(f) PHDOS, (g),(h) $\alpha^2F(\omega)$ and cumulative frequency-dependent EPC λ for C_4Se and *p*-doped C_5Se, respectively.

sufficient-quality projected density of state (PDOS) as shown in Figs. 3(e) and 3(f). It can be clearly seen that a sharp VHS peak appears near the Fermi level, where the contribution of charge density is mainly from C-*p* orbitals. In C_4Se, the principal curvature is electronlike along the *X*-*S* path, while a holelike behavior along the *S*-*Y* path is in the vicinity of the reciprocal space of the saddle point. Therefore, there is a crossover at the *S* point from electronlike to holelike conduction that originates at the VHS. In particular, the appearance of the VHS in C_5Se, located about −0.3 eV below the Fermi level, makes the system intrinsically susceptible to Fermi surface instabilities and has the potential to give rise to a range of unusual phenomena.

By the above hallmark analysis, the electronic energy band structures of C_4Se and C_5Se both exhibit the coexistence feature of Dirac cones and VHS. Similar features have been studied in Lieb lattice and twisted graphene [20,67–69], which are strongly related to the intriguing superconducting state. As mentioned above, C_5Se is a zero band-gap semimetal with no Fermi surface, but its fantastic band structure near the Fermi level creates a favorable condition for tuning the Fermi level. It is well known that doping can be used to induce superconductivity, which has been demonstrated in multiple two-dimensional materials [10,70–72]. Thus, we employed a jellium model and performed simulations of *p*-doped C_5Se (marked as *p*-doped C_5Se) at the carrier density of 1.12×10^{14} cm^{-2}, in which a defect electronic charge is offset by a uniform neutralizing background. We assessed its band structure and DOS, as represented by the green dashed lines in Figs. 3(b) and 3(f), and confirmed that the *p*-doped C_5Se has metallic electronic state and Fermi surface. This configuration of *p*-doped C_5Se provides an ideal platform for further investigation of superconductivity.

D. Superconductivity state

We evaluated the potential superconductivity of C_4Se and *p*-doped C_5Se configurations by calculating their phonon dispersions and relevant electron-phonon coupling parameters. As shown in Figs. 4(a) and 4(b), the ZA, LA, and TA represent the out-of-plane, in-plane longitudinal, and in-plane transverse modes of C_4Se and *p*-doped C_5Se, respectively, which correspond to the three acoustic branches. We find that the acoustic branches are mainly contributed by the vibrations of Se atoms. The out-of-plane vibrations of the Se atoms dominate the low-frequency region, which is lower than 341 and 214 cm^{-1} for C_4Se and *p*-doped C_5Se, respectively, while the in-plane vibrations of the Se atoms dominate the high-frequency region, which is higher than 341 and 214 cm^{-1} for C_4Se and *p*-doped C_5Se, respectively. In both cases, vibrations of C atoms occur over a wide region in the BZ, with the

TABLE I. Coulomb constant μ^*, DOS at the Fermi level N (E_F) (in unit of states/spin/Ry/cell), logarithmic averaged phonon frequency ω_log (in K), electron-phonon coupling constant λ, and T_c (in K) of C_4Se and p-doped C_5Se. Relevant parameters of some known intrinsic superconductors are included for comparison.

Compound	μ^*	$N(E_\mathrm{F})$	ω_log	λ	T_c	Ref.
LiC_6	0.14			0.55	5.9	[73]
B_2C	0.10		314.8	0.92	19.2	[74]
C_6CaC_6	0.21			0.71	6.8	[75]
2H−$NbSe_2$	0.16		189.2	0.91	7.8	[76]
$SnNbSe_2$	0.10	1.58	72.6	1.28	7.0	[77]
Cu-BHT	0.10		51.8	1.16	4.4	[78]
Mo_2B_2	0.10	16.02	344.8	0.49	3.9	[79]
W_2B_2	0.10	12.46	232.4	0.69	7.8	[80]
C_4Se	0.10	8.15	117.1	1.31	11.6	this work
C_5Se	0.10	14.31	133.9	1.13	11.2	this work

in-plane and out-plane phonon modes mainly contributing to the intermediate- and the high-frequency region, respectively.

The phonon dispersions weighted by the magnitude of EPC $\lambda_{q\nu}$ and the phonon density of state (PHDOS) are shown in Figs. 4(c) and 4(f). In both structures, the large EPC strengths mainly originate from the large $\lambda_{q\nu}$ near the Γ point that is associated with the Se soft modes in the acoustic branch. The quantitative analysis shows that approximately 82% of the total EPC in C_4Se can be attributed to low-frequency phonons. The high-frequency phonons dominated by C modes account for the remaining 18%. In the case of p-doped C_5Se, the low-frequency phonons also come from the Se vibrations which contribute 68% of its total EPC, and the high-frequency phonons of C modes contribute the rest. Figures 4(g) and 4(h) show the mode-resolved Eliashberg spectral function $\alpha^2F(\omega)$ and the cumulative frequency-dependent of EPC $\lambda(\omega)$. One can see that the strength of $\lambda_{q\nu}$ in low- and high-frequency regions results in the large peak of the $\alpha^2F(\omega)$ and the growth rate of $\lambda(\omega)$ corresponds to the contribution of $\lambda_{q\nu}$. In comparison, the contribution of intermediate-frequency phonons is negligible.

The logarithmic average frequency ω_log and the superconducting transition temperature T_c of C_4Se and p-doped C_5Se are obtained by using a typical value of the effective screened Coulomb repulsion constant $\mu^* = 0.06{-}0.15$, Eliashberg spectral function $\alpha^2F(\omega)$, and λ. The superconductive parameters of C_4Se and p-doped C_5Se are list in Table I, along with those of some known intrinsic superconductors for comparison. The calculated T_c for C_4Se falls within the range 9.6–13.2 K and that of p-doped C_5Se in the scope of 8.9–12.9 K (see Supplemental Material Fig. S5 [58]). Notably, these values surpass the majority of 2D superconductors. These findings strongly suggest that the integration of Se into C can induce superconductivity, highlighting the potential of Se-doped carbon materials in this regard.

The coexistence of Dirac structure and VHS in C_4Se and C_5Se presents a distinct opportunity to establish a connection between these phenomena and the framework of band-driven superconductivity. Previous studies have suggested that intense electron-electron interaction may result in chiral superconductivity when graphene is doped near the VHS. Here, the Dirac structure along with VHS near E_f plays a crucial role in the emergence of superconductivity. This provides insight into the development of 2D superconducting materials featuring light elements, thereby laying the foundation for further advancements in the field of 2D superconductivity.

E. Topological state

It is known that graphene, as a Dirac material, possesses a nontrivial topological band structure that is intrinsic to its nature. Considering the band structure of C_6Se at the PBE level, which exhibits similarities to graphene [Fig. 5(a)], it is crucial to investigate whether the Dirac cones in C_6Se exhibit any topological properties. However, in contrast to gapless graphene, the HSE band structure of C_6Se reveals a narrow band gap of 0.17 eV [Fig. 5(b)]. To confirm the existence of a genuine Dirac cone, we applied an in-plane biaxial compressive strain to C_6Se and observed that the band gap closes when the strain reaches 9%. At this critical strain, the C_6Se monolayer undergoes a transformation into a Dirac semimetal state, where the Dirac point is precisely located at the Fermi level. A criterion for the topological band is the appearance of a band gap at the Dirac point by spin-orbit coupling (SOC). Here, upon introducing SOC in the strained C_6Se monolayer, the originally degenerate p_z orbitals are now split into two distinct states separated by the Fermi level, resulting in opening a 20-meV band gap (see Supplemental Material Fig. S6 [58]). The emergence of a gap in the energy spectrum due to SOC is a significant indication of the presence of a topological state in C_6Se when subjected to a 9% compressive strain.

Based on our analysis of the fatband decomposition in the vicinity of the Fermi level, it is apparent that these bands primarily originate from the C−p_z orbitals. Consequently, it is feasible and justifiable for modeling these bands utilizing a tight-binding Hamiltonian comprised of C−p_z orbitals:

$$H = U\sum c_i^\dagger c_i + \sum (t_{ij}c_i^\dagger c_j + \mathrm{H.c.}),$$

where U represents the on-site energy, $c_i^\dagger$ and c_i are the annihilation and creation operators of an electron in the ith C−p_z orbital, and t_{ij} is the hopping integral parameter. The on-site energy for all the sites in our TB model was set to 0 eV due to the orbitals all being C−p_z orbitals. We obtained the derived bands of C_6Se under a compressive strain of −9% by using the constructed TB model (see Supplemental Material Fig. S7 [58]), which accords well with the DFT calculations. Then we further calculate the Z_2 invariant to confirm the compressive strain-induced topological nature of C_6Se. The evolutions of Wannier center of charges (WCCs) for the −9% strained C_6Se monolayer at $k_z = 0$ are depicted in Supplemental Material Fig. S8 [58]. Clearly, the evolution line intersects any reference line an odd number of times. This yields a nontrivial topological invariant $Z_2 = 1$ and suggests the existence of nontrivial topological states in C_6Se under a 9% compressive strain. However, considering the weak SOC in C_6Se, it is generally treated as a semimetal except at extremely low temperatures. Notably, one of the striking features of topologies is the existence of robust edge or surface

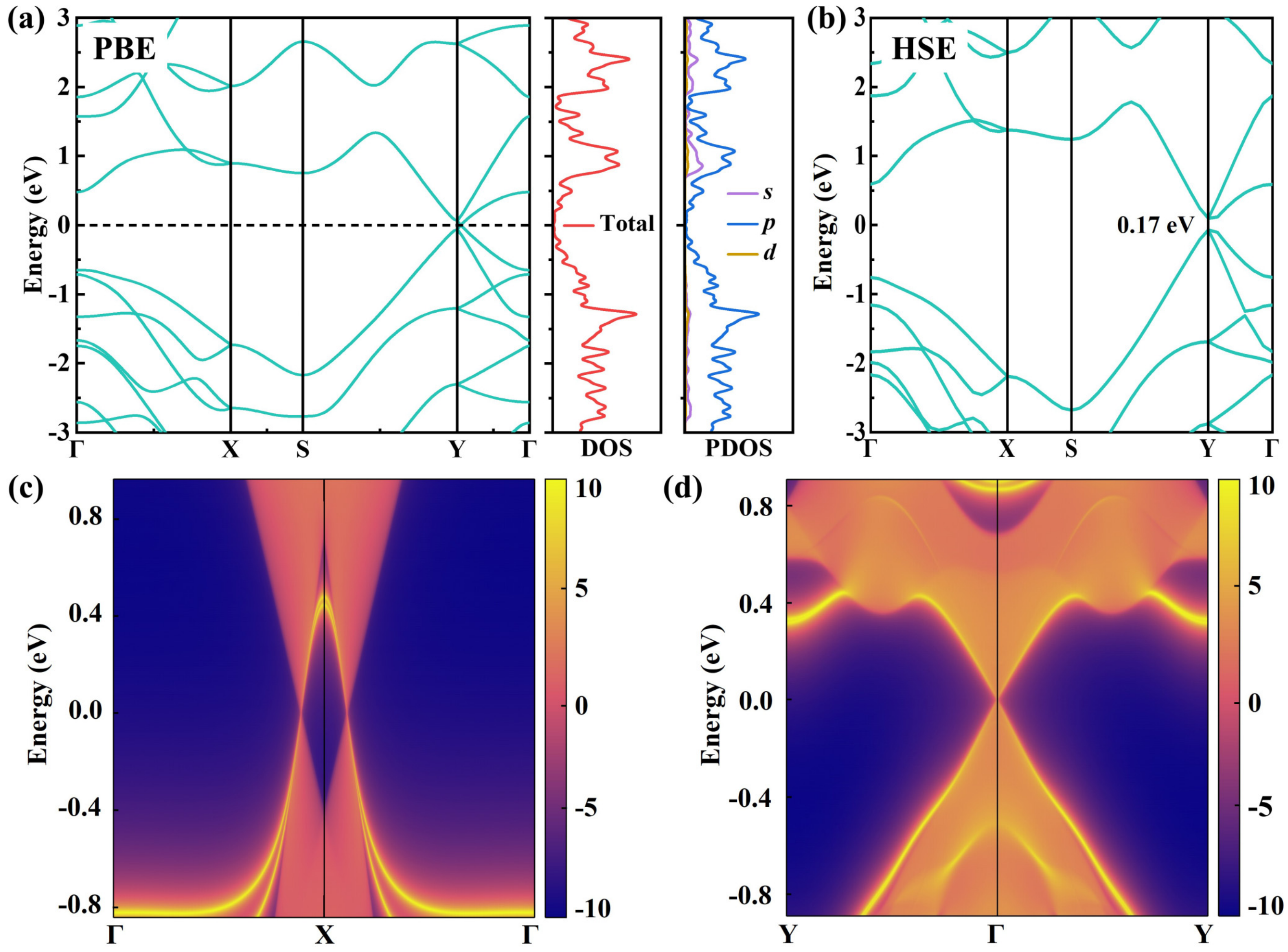

FIG. 5. The electronic band structure and DOS with (a) the PBE functional and with (b) the HSE functional for monolayer C_6Se. (c),(d) The calculated edge states of strained C_6Se in the x and y directions.

states. Therefore, we calculate the edge states of the strained C_6Se monolayer by creating one-dimensional nanoribbons by cutting the sheet. The edge states are calculated for C_6Se nanoribbons in the x direction and y direction, respectively. The results presented in Figs. 5(c) and 5(d) reveal that the edge states of the nanoribbons exhibit gapless characteristics, independent of their orientation, which is consistent with the outcomes of the topological invariant calculation.

IV. CONCLUSIONS

To summarize, using the first-principles swarm-intelligence structure search method, we carried out a detailed study on the geometric structure, phonon stability, electronic properties, as well as electronic states of 2D carbon-rich C_xSe ($x = 4$, 5, and 6) monolayers. Among them, C_4Se and C_5Se monolayers exhibit significant features of Dirac cones and VHS, which have important effects on the electronic and transport properties. By employing *ab initio* calculations and the BCS theory, we investigated their electron-phonon coupling and possible superconductivity. The results show that the former is an intrinsic superconductor with $T_c \sim 11.6\,\mathrm{K}$ and the latter exhibits tunable superconductivity upon doping ($T_c \sim 11.2\,\mathrm{K}$). In both systems, the large EPC strengths mainly originate from the large $\lambda_{q\nu}$ near the Γ point, which is associated with the Se soft modes in the acoustic branch. Additionally, we have discovered a C_6Se crystal with an approximate Dirac-like structure and a narrow band gap of 0.17 eV. Interestingly, under biaxial compressive strain, the C_6Se undergoes a transformation into topological insulator. These intriguing findings could inspire more research on carbon-rich systems doped with Se to explore fascinating physical phenomena.

ACKNOWLEDGMENTS

This work was supported by National Natural Science Foundation of China (NSFC) Grant No. 12164009, the Sichuan Science and Technology program (Grants No. 2022ZYD0024 and No. 2021YFG0228), and the China Postdoctoral Science Foundation (Grant No. 2021M690325).

The authors declare no competing financial interest.

[1] K. S. Novoselov, A. K. Geim, S. V. Morozov, D. Jiang, Y. Zhang, S. V. Dubonos, I. V. Grigorieva, and A. A. Firsov, Electric field effect in atomically thin carbon films, Science **306**, 666 (2004).

[2] K. S. Novoselov, V. I. Fal'ko, L. Colombo, P. R. Gellert, M. G. Schwab, and K. Kim, A roadmap for graphene, Nature (London) **490**, 192 (2012).

[3] D. S. L. Abergel, V. Apalkov, J. Berashevich, K. Ziegler, and T. Chakraborty, Properties of graphene: A theoretical perspective, Adv. Phys. **59**, 261 (2010).

[4] K. I. Bolotin, K. J. Sikes, Z. Jiang, M. Klima, G. Fudenberg, J. Hone, P. Kim, and H. L. Stormer, Ultrahigh electron mobility in suspended graphene, Solid State Commun. **146**, 351 (2008).

[5] K. S. Novoselov, A. K. Geim, S. V. Morozov, D. Jiang, M. I. Katsnelson, I. V. Grigorieva, S. V. Dubonos, and A. A. Firsov, Two-dimensional gas of massless Dirac fermions in graphene, Nature (London) **438**, 197 (2005).

[6] A. A. Balandin, S. Ghosh, W. Bao, I. Calizo, D. Teweldebrhan, F. Miao, and C. N. Lau, Superior thermal conductivity of single-layer graphene, Nano Lett. **8**, 902 (2008).

[7] J. L. McChesney, A. Bostwick, T. Ohta, T. Seyller, K. Horn, J. Gonzalez, and E. Rotenberg, Extended Van Hove Singularity and Superconducting Instability in Doped Graphene, Phys. Rev. Lett. **104**, 136803 (2010).

[8] G. Profeta, M. Calandra, and F. Mauri, Phonon-mediated superconductivity in graphene by lithium deposition, Nat. Phys. **8**, 131 (2012).

[9] S. L. Yang, J. A. Sobota, C. A. Howard, C. J. Pickard, M. Hashimoto, D. H. Lu, S. K. Mo, P. S. Kirchmann, and Z. X. Shen, Superconducting graphene sheets in CaC_6 enabled by phonon-mediated interband interactions, Nat. Commun. **5**, 3493 (2014).

[10] H.-Y. Lu, Y. Yang, L. Hao, W.-S. Wang, L. Geng, M. Zheng, Y. Li, N. Jiao, P. Zhang, and C. S. Ting, Phonon-mediated superconductivity in aluminum-deposited graphene AlC_8, Phys. Rev. B **101**, 214514 (2020).

[11] T. Cea, N. R. Walet, and F. Guinea, Electronic band structure and pinning of Fermi energy to Van Hove singularities in twisted bilayer graphene: A self-consistent approach, Phys. Rev. B **100**, 205113 (2019).

[12] R. Nandkishore, L. S. Levitov, and A. V. Chubukov, Chiral superconductivity from repulsive interactions in doped graphene, Nat. Phys. **8**, 158 (2012).

[13] M. L. Kiesel, C. Platt, W. Hanke, D. A. Abanin, and R. Thomale, Competing many-body instabilities and unconventional superconductivity in graphene, Phys. Rev. B **86**, 020507(R) (2012).

[14] Y. W. Liu, J. B. Qiao, C. Yan, Y. Zhang, S. Y. Li, and L. He, Magnetism near half-filling of a Van Hove singularity in twisted graphene bilayer, Phys. Rev. B **99**, 201408(R) (2019).

[15] H. Yao and F. Yang, Topological odd-parity superconductivity at type-II two-dimensional van Hove singularities, Phys. Rev. B **92**, 035132 (2015).

[16] M. Kang, S. Fang, J.-K. Kim, B. R. Ortiz, S. H. Ryu, J. Kim, J. Yoo, G. Sangiovanni, D. Di Sante, B.-G. Park *et al.*, Twofold van Hove singularity and origin of charge order in topological kagome superconductor CsV_3Sb_5, Nat. Phys. **18**, 301 (2022).

[17] L.-K. Lim, J.-N. Fuchs, F. Piéchon, and G. Montambaux, Dirac points emerging from flat bands in Lieb-kagome lattices, Phys. Rev. B **101**, 045131 (2020).

[18] D. O. Oriekhov, V. P. Gusynin, and V. M. Loktev, Orbital susceptibility of T-graphene: Interplay of high-order van Hove singularities and Dirac cones, Phys. Rev. B **103**, 195104 (2021).

[19] D. Guerci, P. Simon, and C. Mora, Higher-order Van Hove singularity in magic-angle twisted trilayer graphene, Phys. Rev. Res. **4**, L012013 (2022).

[20] V. I. Iglovikov, F. Hébert, B. Grémaud, G. G. Batrouni, and R. T. Scalettar, Superconducting transitions in flat-band systems, Phys. Rev. B **90**, 094506 (2014).

[21] K. Yamazaki, M. Ochi, D. Ogura, K. Kuroki, H. Eisaki, S. Uchida, and H. Aoki, Superconducting mechanism for the cuprate $Ba_2CuO_{3+\delta}$ based on a multiorbital Lieb lattice model, Phys. Rev. Res. **2**, 033356 (2020).

[22] Y. Cao, V. Fatemi, S. Fang, K. Watanabe, T. Taniguchi, E. Kaxiras, and P. Jarillo-Herrero, Unconventional superconductivity in magic-angle graphene superlattices, Nature (London) **556**, 43 (2018).

[23] W. Jiang, S. Zhang, Z. Wang, F. Liu, and T. Low, Topological band engineering of lieb lattice in phthalocyanine-based metal–organic frameworks, Nano Lett. **20**, 1959 (2020).

[24] M. Fortin-Deschênes, R. Pu, Y.-F. Zhou, C. Ma, P. Cheung, K. Watanabe, T. Taniguchi, F. Zhang, X. Du, and F. Xia, Uncovering topological edge states in twisted bilayer graphene, Nano Lett. **22**, 6186 (2022).

[25] R. Mitsuhashi, Y. Suzuki, Y. Yamanari, H. Mitamura, T. Kambe, N. Ikeda, H. Okamoto, A. Fujiwara, M. Yamaji, N. Kawasaki *et al.*, Superconductivity in alkali-metal-doped picene, Nature (London) **464**, 76 (2010).

[26] X. F. Wang, R. H. Liu, Z. Gui, Y. L. Xie, Y. J. Yan, J. J. Ying, X. G. Luo, and X. H. Chen, Superconductivity at 5 K in alkali-metal-doped phenanthrene, Nat. Commun. **2**, 507 (2011).

[27] Y. Kubozono, H. Mitamura, X. Lee, X. X. He, Y. Yamanari, Y. Takahashi, Y. Suzuki, Y. Kaji, R. Eguchi, K. Akaike *et al.*, Metal-intercalated aromatic hydrocarbons: A new class of carbon-based superconductors, Phys. Chem. Chem. Phys. **13**, 16476 (2011).

[28] M. Xue, T. Cao, D. Wang, Y. Wu, H. Yang, X. Dong, J. He, F. Li, and G. F. Chen, Superconductivity above 30 K in alkali-metal-doped hydrocarbon, Sci. Rep. **2**, 389 (2012).

[29] S. Y. Lu, H. Y. Liu, I. I. Naumov, S. Meng, Y. W. Li, J. S. Tse, B. Yang, and R. J. Hemley, Superconductivity in dense carbon-based materials, Phys. Rev. B **93**, 104509 (2016).

[30] X. Chen, Y. Yao, H. Yao, F. Yang, and J. Ni, Topological $p + ip$ superconductivity in doped graphene-like single-sheet materials BC_3, Phys. Rev. B **92**, 174503 (2015).

[31] C. W. Niu, P. M. Buhl, G. Bihlmayer, D. Wortmann, S. Blugel, and Y. Mokrousov, Topological crystalline insulator and quantum anomalous Hall states in IV-VI-based monolayers and their quantum wells, Phys. Rev. B **91**, 201401(R) (2015).

[32] Y. D. Ma, L. Z. Kou, Y. Dai, and T. Heine, Proposed two-dimensional topological insulator in SiTe, Phys. Rev. B **94**, 201104(R) (2016).

[33] E. O. Wrasse and T. M. Schmidt, Prediction of two-dimensional topological crystalline insulator in PbSe mono layer, Nano Lett. **14**, 5717 (2014).

[34] J. W. Liu, T. H. Hsieh, P. Wei, W. H. Duan, J. Moodera, and L. Fu, Spin-filtered edge states with an electrically tunable gap in a two-dimensional topological crystalline insulator, Nat. Mater. **13**, 178 (2014).

[35] Y. C. Wang, J. A. Lv, L. Zhu, and Y. M. Ma, Crystal structure prediction via particle-swarm optimization, Phys. Rev. B **82**, 094116 (2010).

[36] X. Luo, J. Yang, H. Liu, X. Wu, Y. Wang, Y. Ma, S. H. Wei, X. Gong, and H. Xiang, Predicting two-dimensional boron-carbon compounds by the global optimization method, J. Am. Chem. Soc. **133**, 16285 (2011).

[37] Y. C. Wang, J. Lv, L. Zhu, and Y. M. Ma, CALYPSO: A method for crystal structure prediction, Comput. Phys. Commun. **183**, 2063 (2012).

[38] X. Yan, S. C. Ding, X. H. Zhang, A. Bergara, Y. Liu, Y. C. Wang, X. F. Zhou, and G. C. Yang, Enhanced superconductivity in CuH_2 monolayers, Phys. Rev. B **106**, 014514 (2022).

[39] H. Wang, Y. C. Wang, J. Lv, Q. Li, L. J. Zhang, and Y. M. Ma, CALYPSO structure prediction method and its wide application, Comput. Mater. Sci. **112**, 406 (2016).

[40] Y. Chen, X. Feng, J. Chen, X. Cai, B. Sun, H. Wang, H. Du, S. A. T. Redfern, Y. Xie, and H. Liu, Ultrahigh-pressure induced decomposition of silicon disulfide into silicon-sulfur compounds with high coordination numbers, Phys. Rev. B **99**, 184106 (2019).

[41] F. Peng, Y. Sun, C. J. Pickard, R. J. Needs, Q. Wu, and Y. M. Ma, Hydrogen Clathrate Structures in Rare Earth Hydrides at High Pressures: Possible Route to Room-Temperature Superconductivity, Phys. Rev. Lett. **119**, 107001 (2017).

[42] Y. Chen, H. Qin, J. Zhou, T. Yang, B. Sun, Y. Ni, H. Wang, S. A. T. Redfern, M. Miao, H. Lin *et al.*, Unveiling interstitial anionic electron-driven ultrahigh k-ion storage capacity in a novel two-dimensional electride exemplified by Sc_3Si_2, J. Phys. Chem. Lett. **13**, 7439 (2022).

[43] G. Kresse and J. Furthmuller, Efficient iterative schemes for ab initio total-energy calculations using a plane-wave basis set, Phys. Rev. B **54**, 11169 (1996).

[44] P. E. Blöchl, Projector augmented-wave method, Phys. Rev. B **50**, 17953 (1994).

[45] J. P. Perdew, K. Burke, and M. Ernzerhof, Generalized Gradient Approximation Made Simple, Phys. Rev. Lett. **77**, 3865 (1996).

[46] J. Heyd, G. E. Scuseria, and M. Ernzerhof, Hybrid functionals based on a screened Coulomb potential, J. Chem. Phys. **118**, 8207 (2003).

[47] H. J. Monkhorst and J. D. Pack, Special points for Brillouin-zone integrations, Phys. Rev. B **13**, 5188 (1976).

[48] S. Baroni, S. de Gironcoli, A. Dal Corso, and P. Giannozzi, Phonons and related crystal properties from density-functional perturbation theory, Rev. Mod. Phys. **73**, 515 (2001).

[49] P. Giannozzi, S. Baroni, N. Bonini, M. Calandra, R. Car, C. Cavazzoni, D. Ceresoli, G. L. Chiarotti, M. Cococcioni, I. Dabo *et al.*, QUANTUM ESPRESSO: A modular and open-source software project for quantum simulations of materials, J. Phys.: Condens. Matter **21**, 395502 (2009).

[50] P. Giannozzi, O. Andreussi, T. Brumme, O. Bunau, M. Buongiorno Nardelli, M. Calandra, R. Car, C. Cavazzoni, D. Ceresoli, M. Cococcioni *et al.*, Advanced capabilities for materials modelling with Quantum ESPRESSO, J. Phys.: Condens. Matter **29**, 465901 (2017).

[51] K. Lejaeghere, G. Bihlmayer, T. Bjorkman, P. Blaha, S. Blugel, V. Blum, D. Caliste, I. E. Castelli, S. J. Clark, A. Dal Corso *et al.*, Reproducibility in density functional theory calculations of solids, Science **351**, aad3000 (2016).

[52] F. Giustino, Electron-phonon interactions from first principles, Rev. Mod. Phys. **89**, 015003 (2017).

[53] P. B. Allen and R. C. Dynes, Transition temperature of strong-coupled superconductors reanalyzed, Phys. Rev. B **12**, 905 (1975).

[54] A. A. Mostofi, J. R. Yates, Y. S. Lee, I. Souza, D. Vanderbilt, and N. Marzari, wannier90: A tool for obtaining maximally-localised Wannier functions, Comput. Phys. Commun. **178**, 685 (2008).

[55] Q. Wu, S. Zhang, H.-F. Song, M. Troyer, and A. A. Soluyanov, WannierTools: An open-source software package for novel topological materials, Comput. Phys. Commun. **224**, 405 (2018).

[56] B. Lv, X. Hu, X. Liu, Z. Zhang, J. Song, Z. Luo, and Z. Gao, Thermal transport properties of novel two-dimensional CSe, Phys. Chem. Chem. Phys. **22**, 17833 (2020).

[57] M. A. Springer, T. Brumme, A. Kuc, and T. Heine, Electronic structures of two-dimensional PC_6-type materials, arXiv:2109.14899.

[58] See Supplemental Material at http://link.aps.org/supplemental/10.1103/PhysRevB.107.184115 for the configurations, elastic stiffness constants, phonon dispersion curves, AIMD simulation, Young's modulus and Poisson's ratio of predicted carbon-rich selenide monolayers, the atom- and orbital-decomposed band structures of C_4Se and C_5Se, the superconducting critical temperature of C_4Se and p-doped C_5Se as a function of μ^*, the band structure with SOC, TB model derived band, and evolution of WCCs of C_6Se under compressive strain.

[59] S. C. Li, M. Y. Shi, J. H. Yu, S. J. Li, S. L. Lei, L. X. Lin, and J. J. Wang, Two-dimensional blue-phase CX (X = S, Se) monolayers with high carrier mobility and tunable photocatalytic water splitting capability, Chin. Chem. Lett. **32**, 1977 (2021).

[60] Q. Zhang and F. C. Zhang, First-principles study of two-dimensional puckered and buckled honeycomb-like carbon sulfur systems, J. Comput. Electron. **20**, 759 (2021).

[61] J. Guan, Z. Zhu, and D. Tomanek, Phase Coexistence and Metal-Insulator Transition in Few-Layer Phosphorene: A Computational Study, Phys. Rev. Lett. **113**, 046804 (2014).

[62] C. Ataca, M. Topsakal, E. Aktürk, and S. Ciraci, A comparative study of lattice dynamics of three- and two-dimensional MoS_2, J. Phys. Chem. C **115**, 16354 (2011).

[63] H. Zhang, Y. Liao, G. Yang, and X. Zhou, Theoretical studies on the electronic and optical properties of honeycomb BC_3 monolayer: A promising candidate for metal-free photocatalysts, ACS Omega **3**, 10517 (2018).

[64] T. Yu, Z. Zhao, Y. Sun, A. Bergara, J. Lin, S. Zhang, H. Xu, L. Zhang, G. Yang, and Y. Liu, Two-dimensional PC_6 with direct band gap and anisotropic carrier mobility, J. Am. Chem. Soc. **141**, 1599 (2019).

[65] B. Mortazavi, M. Shahrokhi, M. Raeisi, X. Zhuang, L. F. C. Pereira, and T. Rabczuk, Outstanding strength, optical characteristics and thermal conductivity of graphene-like BC_3 and BC_6N semiconductors, Carbon **149**, 733 (2019).

[66] M. Tang, B. Wang, H. Lou, F. Li, A. Bergara, and G. Yang, Anisotropic and high-mobility C_3S monolayer as a photocatalyst for water splitting, J. Phys. Chem. Lett. **12**, 8320 (2021).

[67] L. H. C. M. Nunes and C. Morais Smith, Flat-band superconductivity for tight-binding electrons on a square-octagon lattice, Phys. Rev. B **101**, 224514 (2020).

[68] V. J. Kauppila, F. Aikebaier, and T. T. Heikkila, Flat-band superconductivity in strained Dirac materials, Phys. Rev. B **93**, 214505 (2016).

[69] A. Kerelsky, L. J. McGilly, D. M. Kennes, L. Xian, M. Yankowitz, S. Chen, K. Watanabe, T. Taniguchi, J. Hone, C. Dean *et al.*, Maximized electron interactions at the magic angle in twisted bilayer graphene, Nature (London) **572**, 95 (2019).

[70] E. R. Margine and F. Giustino, Two-gap superconductivity in heavily *n*-doped graphene: *Ab initio* Migdal-Eliashberg theory, Phys. Rev. B **90**, 014518 (2014).

[71] X.-T. Jin, X.-W. Yan, and M. Gao, First-principles calculations of monolayer hexagonal boron nitride: Possibility of superconductivity, Phys. Rev. B **101**, 134518 (2020).

[72] E. Thingstad, A. Kamra, J. W. Wells, and A. Sudbo, Phonon-mediated superconductivity in doped monolayer materials, Phys. Rev. B **101**, 214513 (2020).

[73] B. M. Ludbrook, G. Levy, P. Nigge, M. Zonno, M. Schneider, D. J. Dvorak, C. N. Veenstra, S. Zhdanovich, D. Wong, P. Dosanjh *et al.*, Evidence for superconductivity in Li-decorated monolayer graphene, Proc. Natl. Acad. Sci. USA **112**, 11795 (2015).

[74] J. Dai, Z. Li, J. Yang, and J. Hou, A first-principles prediction of two-dimensional superconductivity in pristine B_2C single layers, Nanoscale **4**, 3032 (2012).

[75] S. Ichinokura, K. Sugawara, A. Takayama, T. Takahashi, and S. Hasegawa, Superconducting calcium-intercalated bilayer graphene, Acs Nano **10**, 2761 (2016).

[76] M. Leroux, I. Errea, M. Le Tacon, S.-M. Souliou, G. Garbarino, L. Cario, A. Bosak, F. Mauri, M. Calandra, and P. Rodière, Strong anharmonicity induces quantum melting of charge density wave in $2H-NbSe_2$ under pressure, Phys. Rev. B **92**, 140303(R) (2015).

[77] P.-J. Chen, T.-R. Chang, and H.-T. Jeng, *Ab initio* study of the $PbTaSe_2$−related superconducting topological metals, Phys. Rev. B **94**, 165148 (2016).

[78] X. M. Zhang, Y. N. Zhou, B. Cui, M. W. Zhao, and F. Liu, Theoretical discovery of a superconducting two-dimensional metal-organic framework, Nano. Lett. **17**, 6166 (2017).

[79] L. Yan, T. Bo, P.-F. Liu, B.-T. Wang, Y.-G. Xiao, and M.-H. Tang, Prediction of phonon-mediated superconductivity in two-dimensional Mo_2B_2, J. Mater. Chem. C **7**, 2589 (2019).

[80] L. Yan, T. Bo, W. X. Zhang, P. F. Liu, Z. S. Lu, Y. G. Xiao, M. H. Tang, and B. T. Wang, Novel structures of two-dimensional tungsten boride and their superconductivity, Phys. Chem. Chem. Phys. **21**, 15327 (2019).